Global Occurrences of Extreme Precipitation and the Madden–Julian Oscillation: Observations and Predictability

CHARLES JONES

Institute for Computational Earth System Science, University of California, Santa Barbara, Santa Barbara, California

DUANE E. WALISER

Institute for Terrestrial and Planetary Atmospheres, State University of New York at Stony Brook, Stony Brook, New York

K. M. LAU

Climate and Radiation Branch, NASA Goddard Space Flight Center, Greenbelt, Maryland

W. STERN

Geophysical Fluid Dynamics Laboratory, Princeton University, Princeton, New Jersey

(Manuscript received 26 February 2004, in final form 25 June 2004)

ABSTRACT

This study investigates 1) the eastward propagation of the Madden–Julian oscillation (MJO) and global occurrences of extreme precipitation, 2) the degree to which a general circulation model with a relatively realistic representation of the MJO simulates its influence on extremes, and 3) a possible modulation of the MJO on potential predictability of extreme precipitation events. The observational analysis shows increased frequency of extremes during active MJO phases in many locations. On a global scale, extreme events during active MJO periods are about 40% higher than in quiescent phases of the oscillation in locations of statistically significant signals.

A 10-yr National Aeronautics and Space Administration (NASA) Goddard Laboratory for the Atmospheres (GLA) GCM simulation with fixed climatological SSTs is used to generate a control run and predictability experiments. Overall, the GLA model has a realistic representation of extremes in tropical convective regions associated with the MJO, although some shortcomings also seem to be present. The GLA model shows a robust signal in the frequency of extremes in the North Pacific and on the west coast of North America, which somewhat agrees with observational studies. The analysis of predictability experiments indicates higher success in the prediction of extremes during an active MJO than in quiescent situations. Overall, the predictability experiments indicate the mean number of correct forecasts of extremes during active MJO periods to be nearly twice the correct number of extremes during quiescent phases of the oscillation in locations of statistically significant signals.

1. Introduction

Severe precipitation events are among the most devastating weather phenomena since they are frequently followed by flash floods and sometimes accompanied by severe weather such as lightning, hail, strong surface winds, and intense vertical wind shear. Consequently, severe precipitation can have significant impacts on societies with losses of human lives and property as well as disruption of infrastructure services. For instance, in the year 2002 alone, the U.S. National Weather Service registered 49 fatalities, 88 injuries, and over $737.5 million dollars in property and crop damages resulting directly from floods in the 50 states, Puerto Rico, Guam, and the Virgin Islands. Likewise, it is noteworthy that even more devastating impacts of severe precipitation are reported in the literature (e.g., Pielke and Downton 2000).

In this study, we refer to extreme precipitation as those events observed at the tails of frequency distribution functions (pdf). In this context, significant research emphasis has been given to identify relationships between low-frequency modes in the coupled ocean–atmosphere system and the occurrence of extremes (Houghton et al. 2001). On interannual time scales, the El Niño–Southern Oscillation (ENSO) is the main mode

Corresponding author address: Dr. Charles Jones, Institute for Computational Earth System Science, University of California, Santa Barbara, Santa Barbara, CA 93106.
E-mail: cjones@icess.ucsb.edu

of variability and several studies have found notable linkages relating ENSO and regional changes in the frequency of extremes (e.g., Bell and Halpert 1998; Mo and Higgins 1998; Cayan et al. 1999; Higgins et al. 2000; Liebmann et al. 2001).

On intraseasonal time scales (20–90 days), the Madden–Julian oscillation (MJO) is the dominant mode of tropical intraseasonal variability and is most active in the boreal winter (Madden and Julian 1994). The influences of the MJO on the patterns of precipitation in the global Tropics and in portions of the extratropics have been well documented. In addition, the MJO strongly influences the precipitation patterns associated with the monsoons in Asia–Australia, and moderately in North and South America (Yasunari 1979; Lau and Chan 1986; Mo 2000; Maloney and Hartmann 1998; Nogués-Paegle et al. 2000; Higgins and Shi 2001; Jones and Carvalho 2002).

More specifically, a few studies have identified important signals of the MJO modulation on heavy precipitation, particularly in the Americas. Mo and Higgins (1998), for instance, examined wet and dry events in California during boreal winter and found that precipitation anomalies over the west coast of North America show a north–south three-cell pattern. Heavy precipitation in California is accompanied by dry conditions over Washington, British Columbia, and along the southeastern coast of Alaska and reduced precipitation over the subtropical eastern Pacific. Wet (dry) events in California are favored during the MJO phase associated with enhanced convection near 150°E (120°E) in the tropical Pacific. Higgins et al. (2000) used gridded 3-day accumulations of precipitation along the west coast of the United States and concluded that extreme events occur at all phases of ENSO, but the largest fraction of these events occurs during neutral winters prior to the onset of El Niño, which tend to be characterized by enhanced tropical intraseasonal activity. Jones (2000) also used gridded station data and found that the frequency of extreme events in California is more common when tropical convective activity associated with the MJO is high, as opposed to periods of quiescent phases of the oscillation. In addition, Jones concluded that a slight preference for a higher number of events in California is observed when convective anomalies associated with eastward propagating events are located in the Indian Ocean. More recently, Bond and Vecchi (2003) obtained statistically significant relationships between the MJO and flooding events in Oregon and Washington during boreal winter.

Likewise, an important modulation of the MJO on extreme precipitation events in South America has been identified as well. Carvalho et al. (2004) determined that the MJO modulates intense South Atlantic convergence zone (SACZ) episodes with persistence longer than 3 days. They additionally found that the MJO phase characterized by suppression of convective activity over Indonesia and enhancement over the central Pacific increases the 95th daily precipitation percentile over north/northeastern Brazil, whereas the opposite features are observed during enhancement of convection over Indonesia and suppression over the central Pacific. Liebmann et al. (2004) investigated the variability of extreme precipitation events and associations with the SACZ and the South American low-level jet. They performed a composite analysis of the MJO relative to anomalous precipitation events and obtained statistically significant variations associated with precipitation both downstream of the jet and in the SACZ. They further speculated that a slowly varying dipole feature is a consequence of the preferred phasing of synoptic waves due to variations of the MJO.

Lastly, other studies include Wheeler and Hendon (2004) who have developed a real-time multivariate index of the MJO and used it to estimate probabilities of extreme weekly precipitation events in Australia. In addition, Barlow et al. (2004, manuscript submitted to *Mon. Wea. Rev.*, hereafter BWLC) determined that daily precipitation in southwest Asia during boreal winter is modulated by MJO activity in the eastern Indian Ocean. They concluded that there is a 55% increase in daily precipitation during suppressed tropical convection in the eastern Indian Ocean associated with the MJO, which affects the distribution of extremes.

The present paper has several objectives. Although previous studies have provided some important understanding of the modulation of the MJO on regional frequencies of extreme precipitation, our current view of this modulation is still quite fragmented. All previous works have concentrated on the influence of the MJO on extreme precipitation over specific geographic locations. Given the planetary scale of the MJO, the first objective of this study is to obtain a global of view of the slow eastward propagation of the MJO during boreal winter and the occurrence of extreme precipitation in the Tropics and extratropics. The results are compared against quiescent periods of the MJO. The next issue addressed in this study relates to the current weakness that most general circulation models (GCMs) have to adequately represent MJO properties (e.g., eastward propagation, period and phase speed, amplitude, etc.), as discussed in more detail in Waliser et al. (2003a,b). In the second objective, we use a GCM that has been shown to have a fairly reasonable representation of the MJO (Waliser et al. 2003b) to investigate how realistic is the modulation of the model MJO on extreme precipitation events. This analysis is performed by comparing the statistical properties of observed and model precipitation and frequency of extremes. Finally, the third objective of this study investigates the modulation of the MJO on the potential predictability of extreme precipitation events, an issue with important operational applications. The paper is organized as follows. Datasets used in the observational analysis are described in section 2. The observational analysis is discussed in section 3. Sections 4 and 5 describe the numerical model and

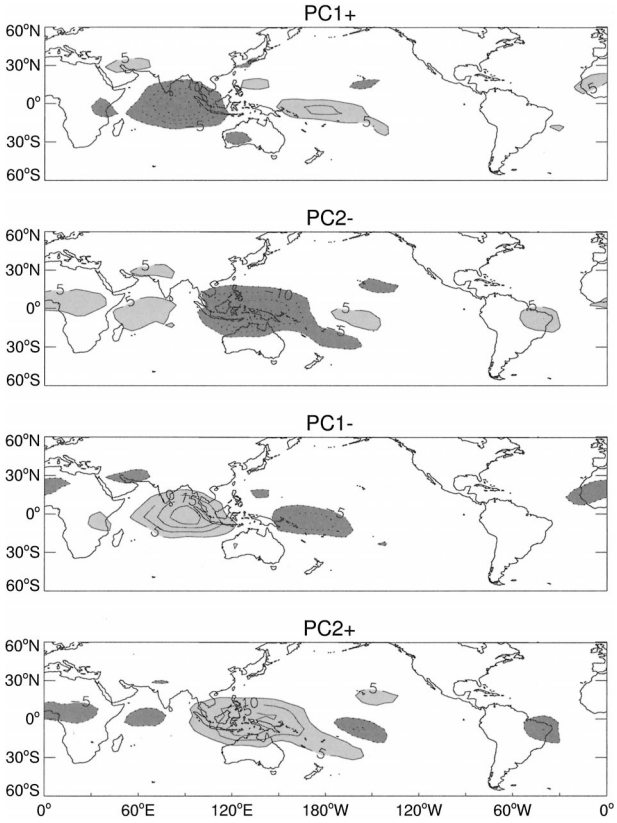

FIG. 1. Composites of 20–90-day OLR anomalies. Light (dark) shading indicates positive (negative) OLR anomalies greater (less) than 5 W m^{-2} (-5 W m^{-2}). Contour interval is 5 W m^{-2} and zero contour is omitted.

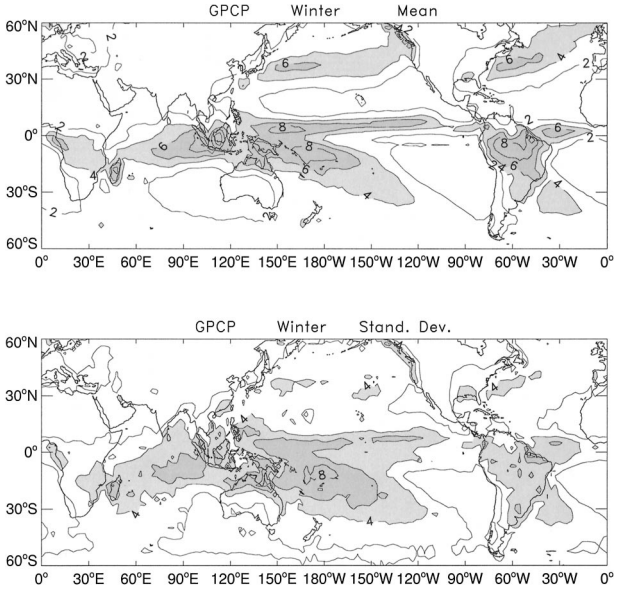

FIG. 2. (top) Mean and (bottom) standard deviation of GPCP precipitation during boreal winter. Contour interval is 2 mm day^{-1}.

experiments. Section 6 examines extreme precipitation in the GCM control run. The predictability of extreme precipitation is investigated in section 7. Section 8 summarizes the study and presents our conclusions.

2. Data

As discussed in the preceding section, previous studies investigated the modulation of the MJO on extreme precipitation using station data and focused on regional aspects. In order to obtain a global view of the MJO influence, we used data from the Global Precipitation Climatology Project (GPCP). Pentads (5-day nonoverlapping averages; 73 pentads per year) are employed for the period 1979–2002 with 2.5° latitude–longitude resolutions. Currently, pentad resolution is necessary to obtain global coverage of precipitation. The analysis is limited to the extended boreal winter (2–6 November through 1–5 May, 851 pentads). The GPCP pentad precipitation analysis is defined by merging several types of observation-based individual datasets such as the GTS gauge observations and estimates inferred from satellite observations of infrared, outgoing longwave radiation, and the Special Sensor Microwave Imager (SSM/I) [see Huffman et al. (1997) and Gruber et al. (2000) for details].

Outgoing longwave radiation (OLR) is used as a proxy for large-scale tropical convection (e.g., Lau and Chan 1986; Waliser et al. 1993; Jones et al. 1998, 2004a). Pentads of OLR (2.5° latitude–longitude) were used for the same period of the GPCP data. To isolate the MJO signal in OLR, time series of OLR were filtered in frequency domain with a fast Fourier transform (FFT) and only periods between 20 and 90 days were retained. The OLR anomalies were additionally filtered in space with a weighted average spatial filter (0.5 for center point and 0.5/8 for the eight neighbor points).

3. Observational results

To begin with, we identified periods of active and inactive MJO using pentads of 20–90-day OLR anomalies in boreal winters using empirical orthogonal functions (EOFs) (60°S/60°N, all longitudes). Prior to EOF calculation, the resolution was degraded (5° × 5° latitude–longitude) and each grid point was scaled by the square root of the cosine of the latitude. Since the number of points in space (72 × 24) is larger than in time (851), the eigenvector calculation was done on the correlation matrix **C** with dimensions 851 × 851. This alternate method of EOF computation (Hirose and Kutzbach 1969) is computationally efficient and ensures that the estimated eigenvalues are stable (Preisendorfer 1988). The first four eigenvalues explain 7.4%, 6.6%, 4.3%, and 3.3% of the total variance. Figure 1 shows composites of 20–90-day filtered OLR anomalies when the amplitudes of the first two principal components (PCs) were above (below) one (minus one) standard

deviation. The number of pentads in each phase is 156 ($PC1^+$), 147 ($PC1^-$), 151 ($PC2^+$), and 135 ($PC2^-$). The typical pattern of eastward propagation of the MJO is clearly observed (Weickmann et al. 1985; Hendon and Salby 1994; Jones et al. 2004a).

To identify quiescent periods of the MJO (i.e., null cases), the amplitudes of the first four PCs were squared, added together, and smoothed with 20 passes of a 1–2–1 filter to create an index of tropical intraseasonal convective activity. Because the index is always positive and has a slight positive skewness, we fitted a gamma frequency distribution and determined the 25th percentile. Null cases were selected when the amplitude of the intraseasonal index is below the 25th percentile (220 pentads).

The statistical properties of GPCP precipitation were analyzed as follows. Figure 2 shows the mean and standard deviation during boreal winters. Intense mean precipitation in tropical regions is located over western Africa extending toward the Indian Ocean and western Pacific, the intertropical convergence zones (ITCZs), and South America. Additionally, mean precipitation is large over the storm tracks in the northern Pacific and Atlantic Oceans. Correspondingly, the variability of precipitation is largest over the Indian Ocean, western Pacific, western North America, and South America. Although the mean and standard deviation are informative parameters of the precipitation variability, other measures are necessary to characterize the tails of the frequency distributions. Because of the skewness in precipitation, gamma frequency distributions were fitted to each time series of precipitation following the maximum likelihood approach (Wilks 1995).

First, we consider the nonzero values of precipitation P_i, $i = 1, N$ in each grid point. We chose this approach to emphasize extreme events with large magnitudes. Next, the sample statistic D is computed:

$$D = \ln(\overline{P}) - \frac{1}{N}\sum_{i=1}^{N} \ln(P_i). \tag{1}$$

Then the shape (α) and scale (β) parameters are estimated by the polynomial approximations:

$$\alpha = \frac{0.500\,087\,6 + 0.164\,885\,2D - 0.054\,427\,4D^2}{D}, \qquad 0 \le D \le 0.5772; \tag{2}$$

$$\alpha = \frac{8.898\,919 + 9.059\,950D - 0.977\,537\,3D^2}{17.797\,28D + 11.968\,477D^2 + D^3}, \qquad 0.5772 < D \le 17.0; \quad \text{and} \tag{3}$$

$$\beta = \frac{\overline{P_i}}{\alpha}. \tag{4}$$

The gamma distribution is thus expressed as

$$f(P) = \frac{(P/\beta)^{\alpha-1}\exp(-P/\beta)}{\beta\Gamma(\alpha)}, \tag{5}$$

where P, α, and $\beta > 0$ and $\Gamma(\alpha)$ is the gamma function. In order to compute the cumulative distribution function, we first scaled the precipitation by $\xi = P/\beta$ and numerically integrated the incomplete gamma function $F(\alpha, \xi)$. Additional details can be found in Wilks (1995).

Before examining the spatial characteristics of the gamma distribution parameters, it is appropriate to illustrate the reasons for developing the approach discussed above. Figure 3 shows examples of histograms of precipitation and the corresponding fitted gamma distribution functions. The locations are chosen to compare small values of α and β (India), large α and small β (storm track in the North Atlantic), small α and large β (western Pacific), and large α and large β (Amazon). The interpretation of the gamma distribution parameters is that small values of the shape parameter α indicate that the distribution is very strongly skewed to the right as is the case in India (note that only the nonzero values of precipitation were used). In contrast, large values of α indicate that the distribution tends to approximate the form of Gaussian distributions such as in the North Atlantic. Note, however, that the asymmetry in the tails is still quite evident. The scale parameter β represents the ''stretch'' or ''squeeze'' in the gamma density function to the right or left (Wilks 1995).

The 75th percentiles from the fitted gamma distribution approach are 0.560, 5.624, 11.091, and 11.838 mm day^{-1}, and the numbers of data points above the 75th percentile are 68, 206, 232, and 195 (i.e., extreme values). Another approach to determine extreme precipitation could be to simply rank the nonzero precipitation values and select the largest 25% values. In that approach, the 75th percentiles for these examples would be 0.457, 5.589, 11.654, and 11.602 mm day^{-1}, respectively. In that situation, the numbers of extreme values would be 77, 212, 212, and 211. The differences between the two approaches to characterize extreme values are 11.7%, 2.8%, −9.4%, and 7.6%, respectively. It is clearly evident that differences can be quite important when precipitation is strongly skewed (e.g., India). Furthermore, although some of the differences may appear small, they can still be important when one is dealing with rare events. This example indicates the

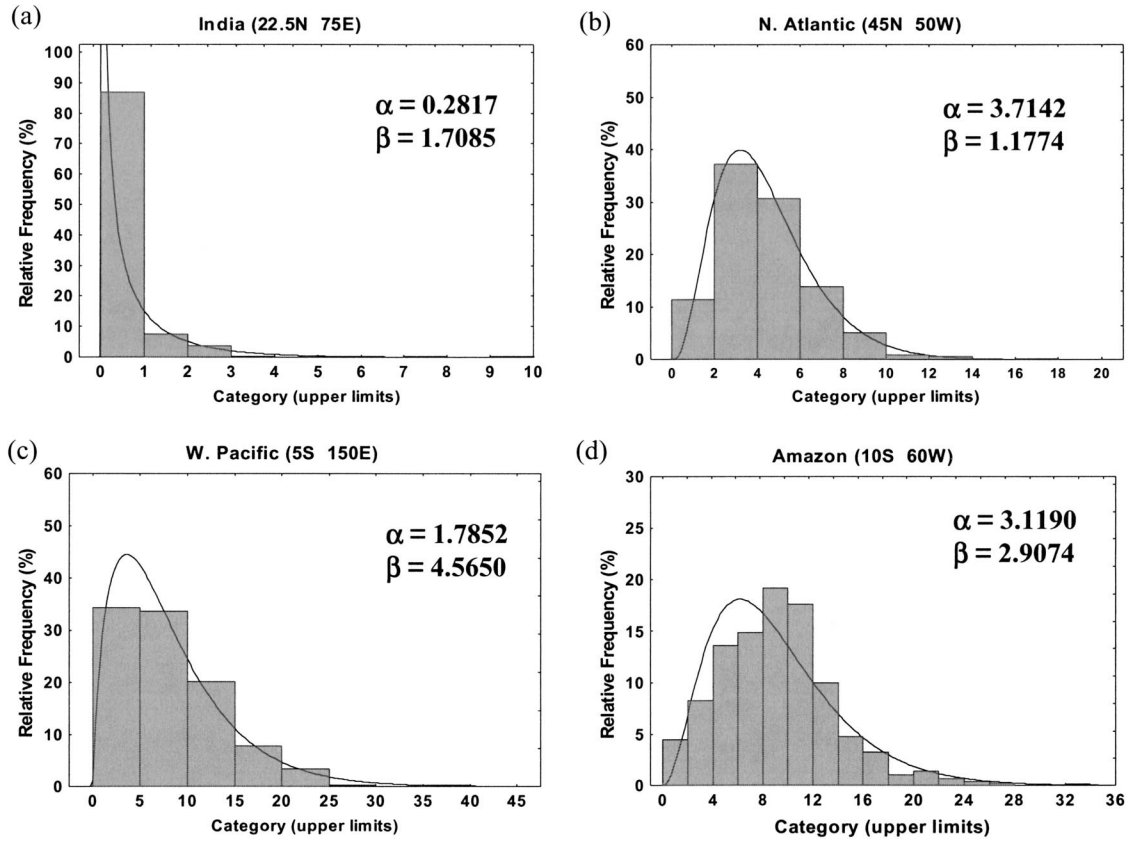

FIG. 3. Examples of frequency distributions of precipitation. Solid lines indicate the adjusted gamma frequency distribution and the corresponding α and β parameters.

need to adequately fit frequency distribution functions to the precipitation data to characterize extreme values. This is especially important in this work since one of the main objectives is to investigate the modulation of the MJO on occurrences of extremes across different climatic precipitation regimes.

Figure 4 shows α and β parameters for the GPCP precipitation in boreal winter. Somewhat expectedly, $\alpha > 2$ is observed over regions with frequent precipitation such as tropical Africa, Indonesia, the Amazon, the ITCZ, and the storm tracks in both hemispheres, indicative of less skewed pdfs. Dry regions, on the other hand, typically exhibit $\alpha < 1$. Extensive regions with large values of β (>5 mm day^{-1}) are observed in the eastern Indian Ocean, South Pacific convergence zone (SPCZ), and eastern South America.

In this study, we define an extreme event as when the GPCP precipitation exceeds the 75th percentile of the gamma pdf. Increasing the percentile value emphasizes dramatic extremes but, on the other hand, results in small samples to derive robust results. Thus, for each grid point, we counted the number of extreme events and divided by the total sample (851 pentads). This measure gives the likelihood of extreme precipitation during winter. Note that, since the gamma distribution was fitted to nonzero values of precipitation, the frequency of extremes is not always equal to 25% (Fig. 5). It is interesting to note that several regions display over 25% frequency of extremes such as the tropical Indian Ocean and western Pacific and the ITCZ. South America displays large values over the northern and southeastern regions, whereas North America has high values over the northwestern and eastern coasts. High values are also seen over Europe and parts of Asia.

The influence of the MJO on extreme precipitation was investigated by computing the proportions of extremes in the four MJO phases (PC1$^+$, PC1$^-$, PC2$^+$, PC2$^-$): $P1_k = h_k/N1_k$, where $k = 1, 4$, h_k is the number of events and $N1_k$ is the sample size (156, 147, 151, 135). Similarly, the proportion of extremes during quiescent MJO periods is $P2 = h/N2$, where the null sample size is 220 pentads. We performed a one-tailed statistical test such that the null hypothesis was $H0$: $P1_k = P2$ and the alternative is $H1$: $P1_k > P2$. The test statistic used is

$$Z_k = \frac{P1_k - P2}{\sigma}, \tag{6}$$

$$\sigma = \sqrt{PQ\left(\frac{1}{N1_k} + \frac{1}{N2}\right)}, \qquad P = \frac{N1_k P1_k + N2P2}{N1_k + N2},$$

$$Q = 1 - P. \tag{7}$$

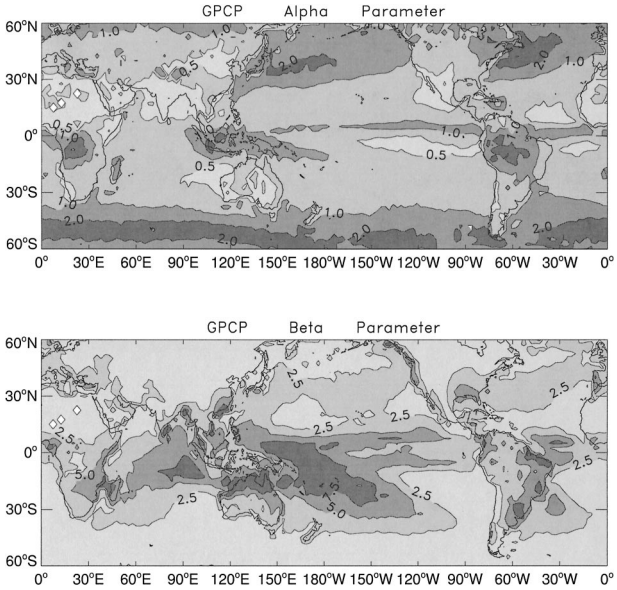

FIG. 4. (top) Shape (α) parameter of gamma probability distribution functions fitted to GPCP precipitation during boreal winter. Shading indicates values as $0.0 \leq \alpha < 0.5$ (light), $0.5 \leq \alpha < 1.0$ (medium light), $1.0 \leq \alpha < 2.0$ (dark), and $\alpha \geq 2.0$ (heavy). (bottom) As in top panel but for scale (β) parameter. Shading indicates values as $0.0 \leq \beta < 2.5$ (light), $2.5 \leq \beta < 5.0$ (medium light), $5.0 \leq \beta < 7.5$ (dark), and $\beta \geq 7.5$ (heavy). Units are in mm day^{-1}.

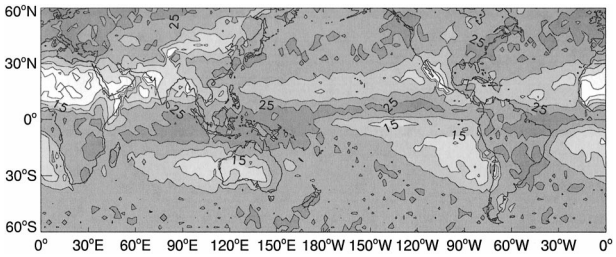

FIG. 5. Frequency of extreme precipitation from GPCP dataset during boreal winter. Extremes are defined when precipitation is above the 75th percentile. First contour is at 5% and interval is 5%.

Note that the parameters in (6) and (7) are functions of space, but additional indexes are omitted to simplify the notation. Figure 6 shows the test statistic Z_k obtained for each MJO phase and, for display clarity, only grid points that exceeded 90% ($Z_k > 1.645$, light shading) and 95% ($Z_k > 1.960$, dark shading) significance levels are shown. Note that our confidence is likely greater for large regions than at isolated grid points that passed the statistical tests. A large region with statistically significant Z_k values extends from Africa toward the Indian Ocean (Fig. 6, top left), consistent with the enhanced tropical convective anomalies associated with the MJO (Fig. 1). This evidently indicates that extreme precipitation in the tropical Indian Ocean is more likely to occur when there is large-scale organized convection associated with the MJO than in inactive episodes. More importantly, other regions also show more extremes dur-

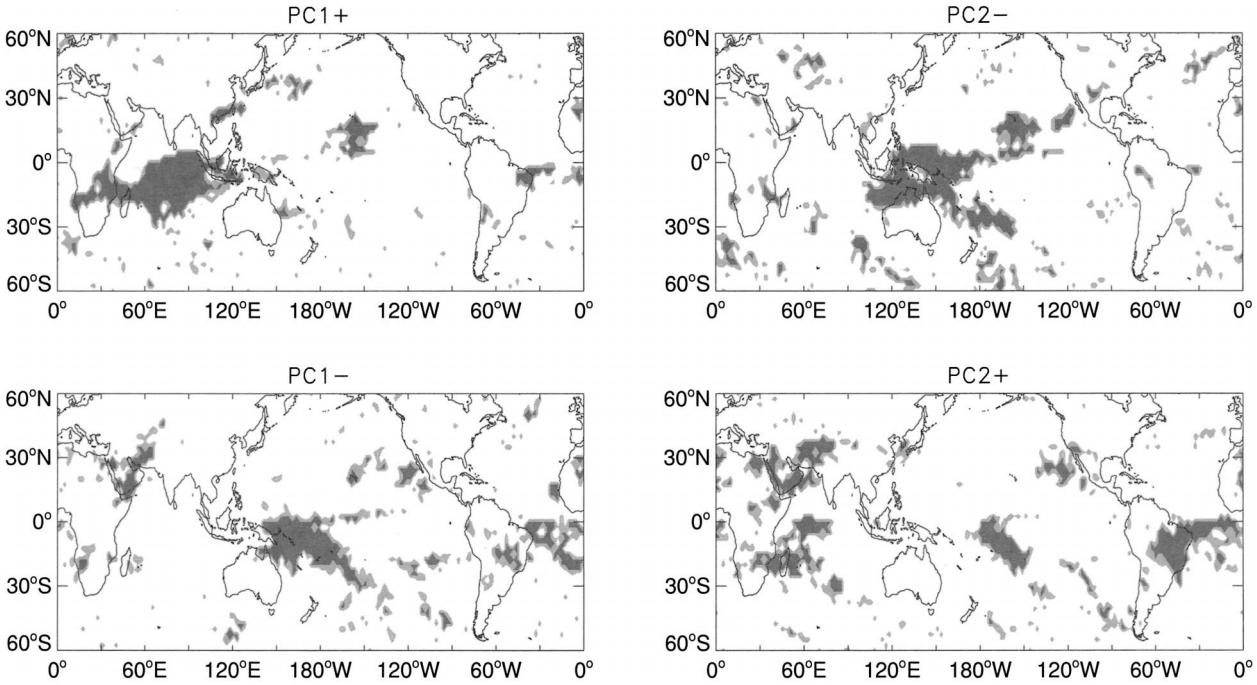

FIG. 6. Test statistic Z_k obtained from GPCP data analysis. Light (heavy) shading indicates regions statistically significant at the 90% (95%) level where extreme precipitation is more frequent in the corresponding MJO phase than during quiescent periods of the oscillation. Only positive Z_k values are shaded (see text for further details).

ing an active MJO, such as eastern Asia and Japan, a reasonably large area encompassing the Hawaiian Islands, and northeastern Brazil. In contrast, during active MJO periods with convective activity anomalies over Indonesia (PC2$^-$), extremes are more frequent over that location (Fig. 6, top right). That region seems to extend northeastward toward the Hawaiian Islands and North America, which is likely related to the MJO modulation on moisture plumes in the ''pineapple express'' region (Higgins et al. 2000).

When convective anomalies propagate farther eastward (PC1$^-$), extreme events are more frequent in the western Pacific (Fig. 6, bottom left). It is interesting to observe that in this MJO phase, suppressed convection is located over the tropical Indian Ocean (Fig. 1) and another region with high probability of extremes extends from Saudi Arabia toward Afghanistan (Fig. 6 bottom left). This is consistent with the BWLC study, which used daily precipitation from stations in Afghanistan. Furthermore, during this phase of the MJO, extremes start to become more frequent in southern Brazil and in the tropical Atlantic Ocean. Subsequently, the MJO propagates farther eastward such that suppressed convection is located over Indonesia, enhanced convection develops over the western Indian Ocean, and the remaining convective anomalies are over the central Pacific (Fig. 1; PC2$^+$). In this situation, extremes are collocated with convective anomalies over the Indian Ocean and central Pacific (Fig. 6, bottom right). The region of high Z_k values in the Middle East enlarges and now encompasses several countries such as Egypt, Turkey, Saudi Arabia, Iran, Afghanistan, Pakistan, and western China. Likewise, a broad region in South America and the tropical Atlantic indicates that extremes are more frequent in this phase of the MJO. This is also consistent with Carvalho et al. (2004), who used precipitation from surface stations in Brazil. Finally, another region with more extremes during the active MJO is seen off the west coast of North America extending into southern California. It is worth mentioning that the MJO modulation on precipitation extremes in western North America obtained with surface data (Mo and Higgins 1998; Higgins et al. 2000; Jones 2000; Bond and Vecchi 2003) is not entirely seen in the GPCP analysis. Part of the reason can be attributed to the time resolution of pentads (GPCP) and station data (daily totals). Also, the coarse horizontal resolution in the GPCP data may be unable to capture the effects of important topographic mesoscale circulations responsible for heavy precipitation in those locations.

To gain further insight into the differences in the proportions of extremes during active MJO and quiescent periods, we computed the average $P1_k$ and $P2$ over the grid points that passed the 90% significance test shown in each panel in Fig. 7. For each phase, the minimum and maximum values of $P1_k$ and $P2$ are also displayed in Fig. 7. It is clearly seen that the mean $P1_k$ in each MJO phase is about 40% higher than in the quiescent periods of the oscillation in those locations in which the MJO influence is statistically significant.

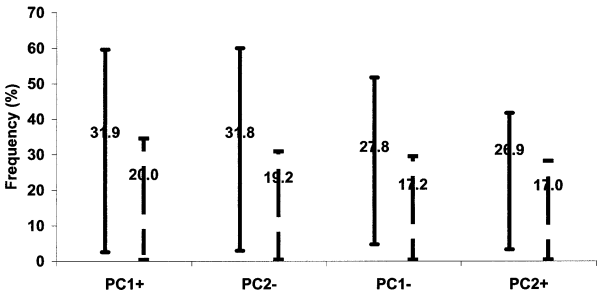

FIG. 7. Mean frequency of extreme precipitation. Numbers in the middle of the bars indicate the average $P1_k$ (solid bar) and $P2$ (dashed bar) over the grid points that passed the 90% significance test shown in each panel in Fig. 6 [see (6) and (7)]. For each phase, the minimum and maximum values of $P1_k$ and $P2$ are shown as the extremes in the vertical bars.

4. Numerical model

To investigate the influence of the MJO on the potential predictability of extreme precipitation events, we used the exact same model described in Waliser et al. (2003a,b). The numerical model is the National Aeronautics and Space Administration (NASA) Goddard Laboratory for the Atmospheres (GLA) general circulation model (GCM); an earlier version is described in Kalnay et al. (1983). Modifications included increased vertical resolution and several changes in the parameterizations of radiation, convection, cloud formation, precipitation, vertical diffusion, and surface processes (Sud and Walker 1992; Phillips 1996). The horizontal representation uses surface finite differences ($4° \times 5°$ latitude–longitude) energy and momentum-conserving A grid (Arakawa and Schubert 1974). The vertical domain has 17 unequally spaced sigma levels from the surface to 12 hPa. Seasonal and diurnal cycles in solar forcing are simulated following Harshvardhan et al. (1987). The formulation of convection follows the scheme of Arakawa and Schubert (1974) and Lord and Arakawa (1980). The model orography is based on the $1° \times 1°$ topographic height data of Gates and Nelson (1975), which has been area averaged over the 40×50 grid boxes. The resulting orography is smoothed with a 16th-order Shapiro (1970) filter and a Fourier filter poleward to 60° latitude.

In general, the GLA model performed very well with respect to its representation of the MJO in the Slingo et al. (1996) Atmospheric Model Intercomparison Project (AMIP) study. Further comparison by Sperber et al. (1996) revealed that the GLA, along with the U.K. Met Office (UKMO) model and version 2 of the Community Climate Model (CCM2), exhibited variability closely resembling the observed features of the MJO. In particular, the GLA model tended to produce a better representation of the eastward propagation of convec-

tion and its associated cyclonic and anticyclonic circulation anomalies when compared to the UKMO model.

5. Experimental framework

A 10-yr control run was first performed with the GLA model using climatological sea surface temperatures. Daily precipitation averages (four 6-h values) for extended boreal winters are used (4 November–2 May, total: 1620 days). Furthermore, a series of twin predictability experiments were also performed. Initial conditions were selected for a number of MJO events from the control run. The selected MJO events were chosen based on an extended empirical orthogonal function analysis (EEOF) of precipitation data from the region 32°N–32°S, 32.5°E–92.5°W. This region encompasses most of the variability in precipitation associated with the MJO (e.g., Lau and Chan 1986; Wang and Rui 1990; Jones et al. 2004a). To isolate the intraseasonal time scale, daily data were bandpassed with a 30–90-day Lanczos filter (Duchon 1979). EEOF analysis, using temporal lags from -7 to $+7$ pentads, was then performed on pentad averages of the bandpassed precipitation. The first (second) mode contains 6.0% (5.9%) of the variance of the time-lagged sequences of the bandpassed data. The model precipitation variance in the 30–90-day band represents 33% (28%) of the seasonal variance in the Tropics (extratropics).

Candidate MJO events to use for initial conditions were chosen from the amplitude time series associated with model EEOF modes 1 and 2 after having been interpolated to daily values. Given that these modes capture the propagation of the MJO, selecting periods when the amplitude of these time series is large will capture strong, propagating MJO events. The two series have maximum correlation (0.95) at a lag of $\pm\sim$12 days, indicating a dominant period of about 50 days (see Waliser et al. 2003a).

For each of these four phases, the 15 events with the greatest amplitudes for each of the four phases were selected. In order to compare high MJO activity to those with little or no MJO activity, 15 initial conditions were also chosen from periods in which neither of the above modes were strongly exhibited in the model atmosphere. The amplitude time series for EEOF modes 1–4 for the Northern Hemisphere winter, along with the analogous four series for the summer, were squared, added together, and then smoothed with a 51-day ($\sim$MJO cycle) running filter. This combined series gives a bulk index of generalized intraseasonal activity. The 15 events during boreal winter with the lowest values of this index were selected to represent low MJO activity conditions with the additional criteria that the events had to occur at least 10 days apart. The latter criterion was applied to get a sample of distinct atmospheric states of low MJO activity (see Waliser et al. 2003b). Hereafter, these cases will be referred to as null events.

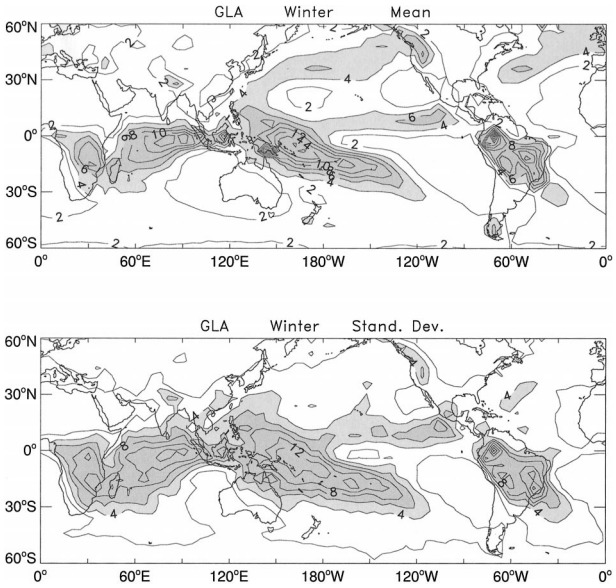

FIG. 8. (top) Mean and (bottom) standard deviation of precipitation from the 10-yr GLA model control run during boreal winter (4 Nov–2 May; 1620 days). Contour interval is 2 mm day^{-1}.

Two perturbations were performed for the 75 cases selected [(4 MJO phases + null phase) $\times$ 15 events]. The initial condition perturbations were computed as follows. Given the day of the month that the initial condition occurs, day-to-day root-mean-square (rms) differences were computed (on the model's sigma surfaces) from the daily averaged values of the model's four prognostic variables (u, v, T, q) for that particular month. This process was meant to provide some spatial structure to the perturbation, whereby larger day-to-day variability would translate into more uncertainty in the initial conditions. These rms values were then multiplied by a random number scaled between -0.1 and 0.1 for the first set of perturbations and -0.2 and 0.2 for the second set. These ''errors'' were then added to the original initial condition's prognostic values to produce alternative initial conditions. For each alternative initial condition, the model was integrated for 90 days.

6. Numerical model results

In this section, we examine the degree to which the GLA model simulates the observed precipitation variability and the modulation of the MJO on extreme events. Figure 8 shows the mean and standard deviation of precipitation from nine winter seasons (4 November–2 May: 1620 days) from the control run simulation. In order to compare with the GPCP variability, the GLA data were first resampled into pentads. A comparison with GPCP (Fig. 3) reveals that the GLA captures fairly well the mean spatial patterns of precipitation in the main tropical convergence zones, although the model precipitation is twice as large in some locations in the

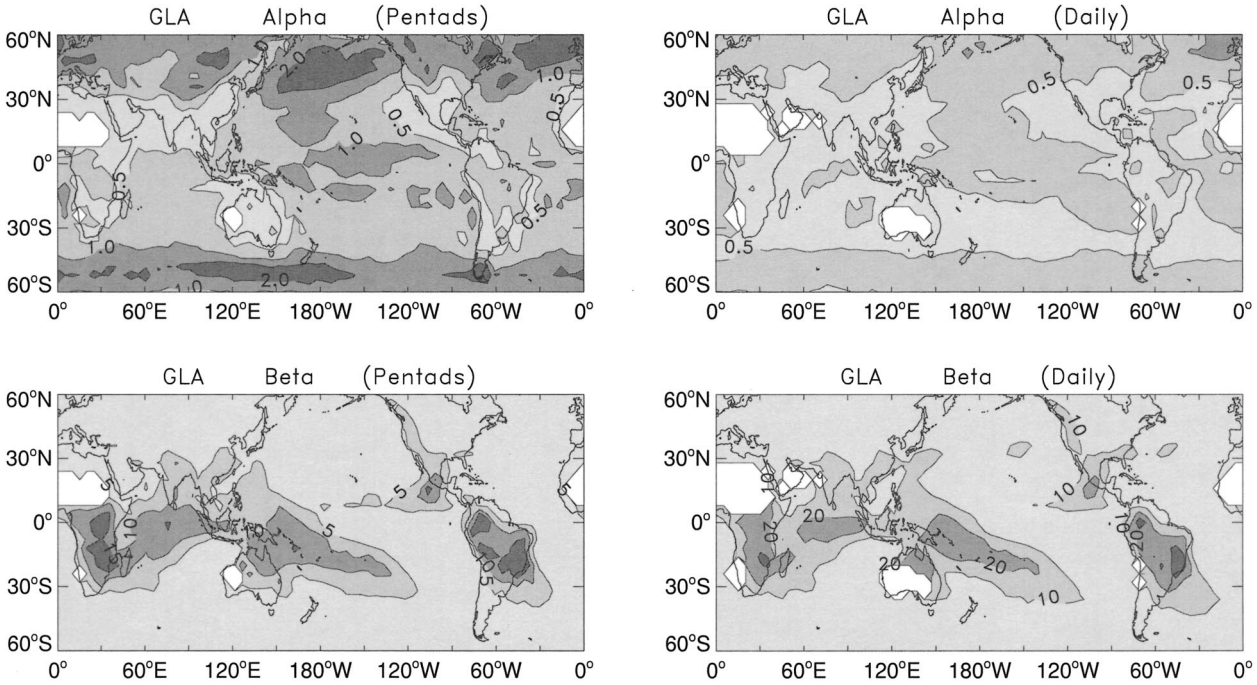

FIG. 9. As in Fig. 4 but for shape (α) and scale (β) parameters of gamma probability distribution functions fitted to the GLA 10-yr control run during boreal winter. Panels on the left are derived for precipitation in pentads and on the right for daily resolution. Shading ranges for α are $0.0 \le \alpha < 0.5$ (light), $0.5 \le \alpha < 1.0$ (medium light), $1.0 \le \alpha < 2.0$ (dark), and $\alpha \ge 2.0$ (heavy). Precipitation in pentad resolution: $0.0 \le \beta < 5.0$ (light), $5.0 \le \beta < 10.0$ (medium light), $10.0 \le \beta < 15.0$ (dark), and $\beta \ge 15.0$ (heavy). Precipitation in daily resolution: $0.0 \le \beta < 10.0$ (light), $10.0 \le \beta < 20.0$ (medium light), $20.0 \le \beta < 30.0$ (dark), and $\beta \ge 30.0$ (heavy). Units for β are in mm day^{-1}.

Indian Ocean, Indonesia, and South America and the Atlantic ITCZ appears weaker than observed. The storm track regions in the North Pacific and Atlantic Oceans are well simulated. The variability in the GLA precipitation (Fig. 8 bottom) is considerably higher than in the GPCP data.

Further understanding can be obtained by comparing the parameters of gamma pdfs of the GLA precipitation with GPCP data. Gamma pdfs were fitted to the GLA data following the same methodology previously explained. However, since the GPCP data is in pentads, we fitted gamma pdfs to GLA data in pentads (324) as well as daily resolution. Note that precipitation data in pentads tends to be less skewed than with daily resolution since days with zero precipitation are more often averaged with nonzero data. A comparison between α and β parameters from the GLA precipitation in pentads (Fig. 9, left column) and the GPCP (Fig. 4) reveals quite realistic patterns in the storm tracks of both hemispheres. In the Tropics, however, the GLA precipitation is more skewed to the right than the GPCP data. By contrast, the GLA β parameter shows similar patterns in several places in the tropical region, although the excessive model precipitation in Colombia and Ecuador is again noted. The small values of α and large values of β from Africa toward the western Pacific and over South America indicate that the daily GLA precipitation (Fig. 9, right column) is skewed and stretched to the right. It is also interesting to observe that in the storm track regions, the daily GLA precipitation is less skewed than in the Tropics, indicative of uniform precipitation in time.

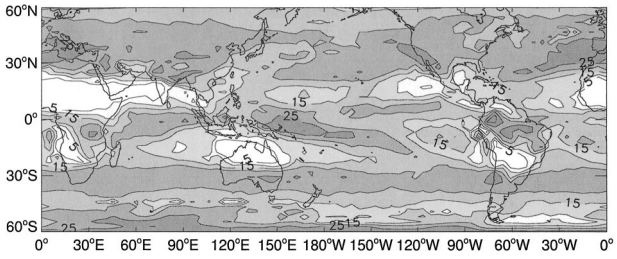

FIG. 10. Frequency of extreme precipitation in the GLA 10-yr control run during boreal winter. Extremes are defined when daily precipitation is above the 75th percentile. First contour is at 5% and interval is 5%.

We define an extreme event when the daily GLA precipitation exceeds the 75th percentile of the gamma pdf. The use of GLA daily precipitation (instead of pentads) is necessary to obtain samples large enough to draw robust conclusions. Thus, for each grid point, we counted the number of extreme events and divided by the total sample (1620 days), to obtain the likelihood of extreme precipitation during winter (Fig. 10). Somewhat similar to the GPCP data, several regions display over 20% frequency of extremes such as the tropical Indian Ocean, western Pacific, and the storm tracks. South

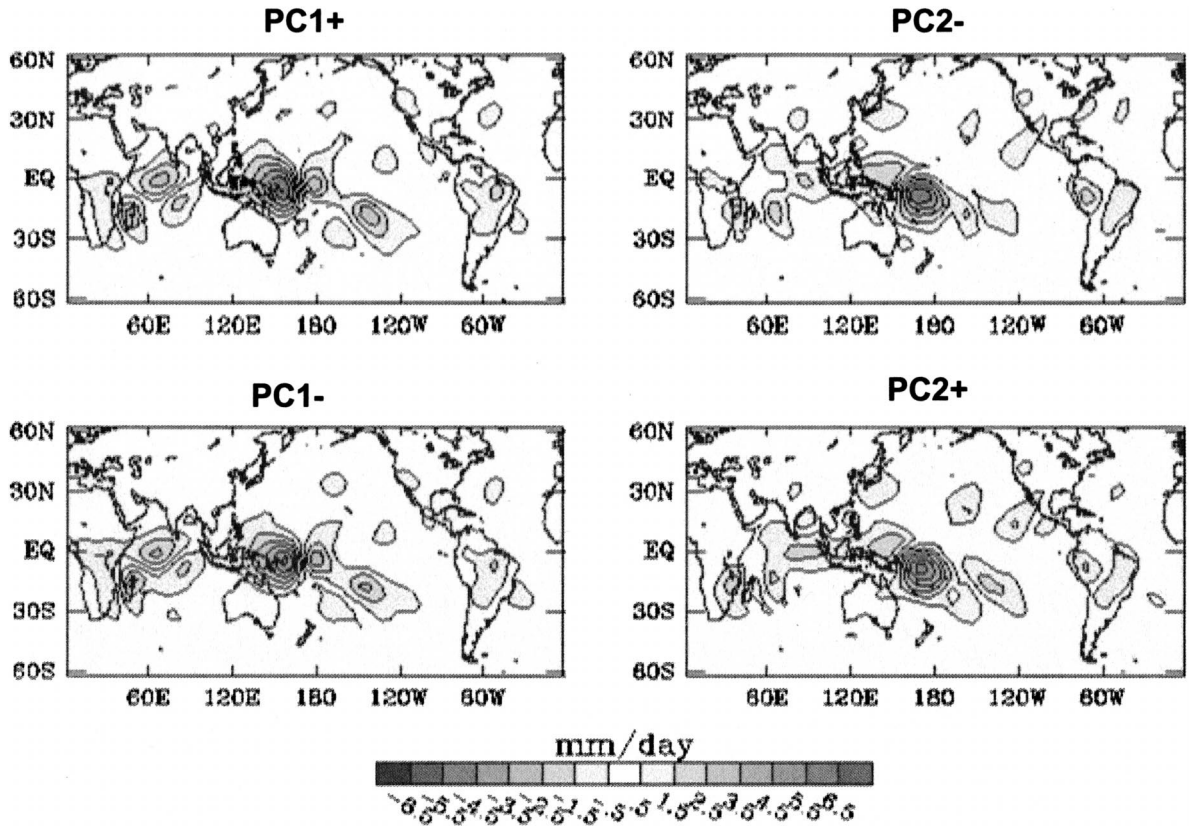

FIG. 11. Composites of filtered (30–90 days) daily precipitation anomalies from the GLA model. Composites were computed from the 15 initial conditions selected to perform predictability experiments during active MJO cases.

America displays large values over Colombia and Ecuador, the Amazon, and southeastern Brazil, while North America has high values over the western coast of the United States.

To illustrate the MJO variability in the GLA model, Fig. 11 shows composites of 30–90-day rainfall anomalies for the 15 initial conditions selected for the four MJO phases based on the amplitudes of the first two EEOF modes. The four phases are indicated as Indian, Maritime Continent, western Pacific and central Pacific. When the model PC1 is positive (negative), precipitation tends to be high in the western Indian (western Pacific) Ocean, and when PC2 is negative (positive), precipitation tends to be high in the eastern Indian (central Pacific Ocean/South Pacific convergence zone) Ocean. Periods of high MJO activity in the control run were selected when the amplitudes of the first two principal components (PC) were above (below) one (minus one) standard deviation. The number of days in each phase was 244 (PC1+), 247 (PC1−), 265 (PC2−), and 259 (PC2+). Similarly, quiescent periods of the MJO (null cases) were selected by taking the amplitudes of the first four PCs squared, added together, and smoothed with a 51-day running filter to create an index of tropical intraseasonal convective activity. Null cases were chosen when the amplitude of the index was below the 25th percentile (404 days).

The modulation of extreme precipitation by the MJO in the GLA model was investigated by computing the proportions of extremes ($P1_k$) in the four MJO phases as well as in the null cases ($P2$). As before, the test statistic Z_k was computed for each MJO phase and the one-tailed statistical test was performed. Figure 12 shows Z_k values that passed the 90% (light shading) and 95% (heavy shading) significance levels. When convective activity anomalies associated with the MJO are in the Indian Ocean (Fig. 11), extremes are more frequent in that location than during quiescent cases (Fig. 12, top left). Note, however, that the GLA model seems to have fewer extremes in the eastern Indian Ocean than what is observed in the GPCP data. Other regions with more extremes include the subtropical Pacific, a broad region extending over North America, and some small areas in South America. Extremes are more frequent in the Maritime Continent during MJO cases than in null situations (Fig. 12, top right). Furthermore, away from the convective region, other locations also exhibit more extremes associated with the MJO, such as northwest and northeast areas in the Pacific, the North Atlantic, and South America. More extremes are found in the

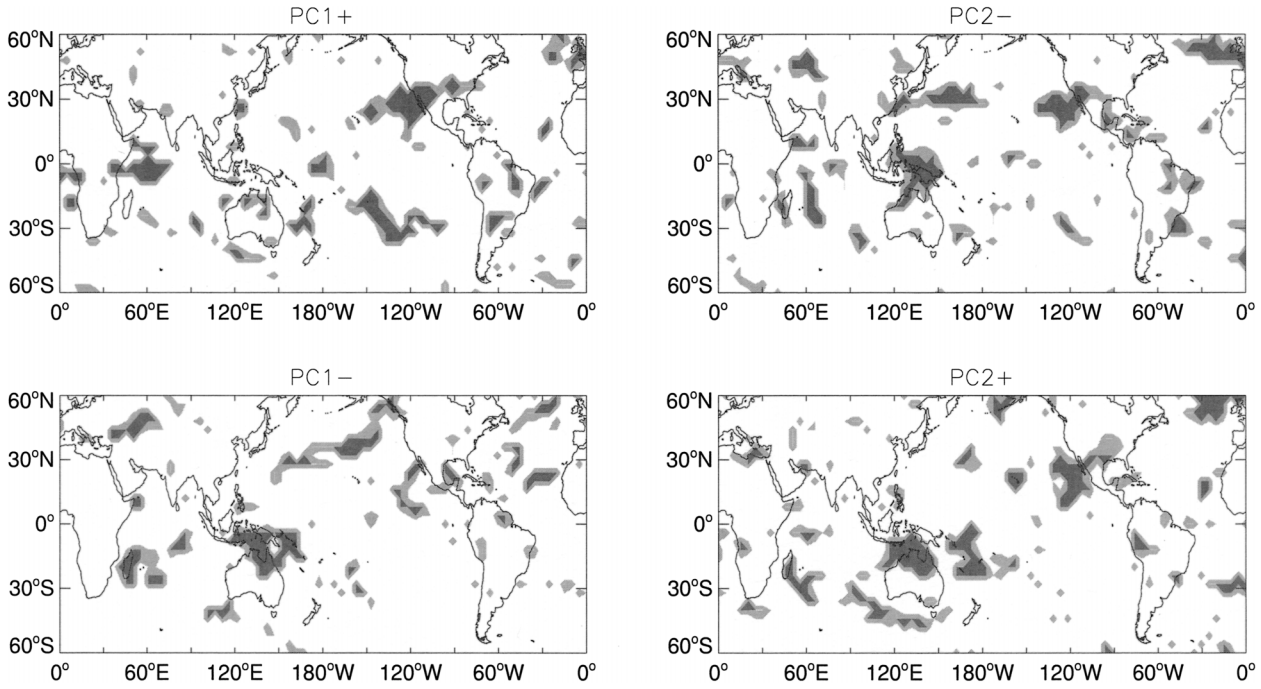

FIG. 12. Test statistic Z_k obtained from the GLA 10-yr control run. Light (heavy) shading indicates regions statistically significant at the 90% (95%) level where extreme precipitation is more frequent in the corresponding model MJO phase than during quiescent periods of the oscillation. Only positive Z_k values are shaded (see text for further details).

western Pacific (Fig. 12, bottom left) when there is enhanced convection associated with the MJO. The model MJO in this situation also seems to modulate more occurrences of extremes in the northern Pacific, likely as an influence on model synoptic disturbances in the jet stream region. Subsequently, as convective anomalies associated with the MJO propagate in the central Pacific, extremes are more frequent in that region (Fig. 12, bottom right). Notable to observe is also the large area of extremes just off the west coast of North America.

Figure 13 shows the average $P1_k$ and $P2$ over the grid points that passed the 90% significance test shown in each panel in Fig. 12. For each phase, the minimum and maximum values of $P1_k$ and $P2$ are also displayed. Unlike the observed relations found with the GPCP data (Fig. 7), there are no remarkable differences in the mean number proportions of extremes. Part of the reason is that the proportions of extremes in the centers of convective activity associated with the MJO in the GLA model are not as extensive as in the observations (cf. Figs. 6 and 12). Nevertheless, the maximum values of $P1_k$ in the GLA model are higher than $P2$, which suggests that the model is able to simulate a higher number of extremes in active MJO periods than in quiescent periods.

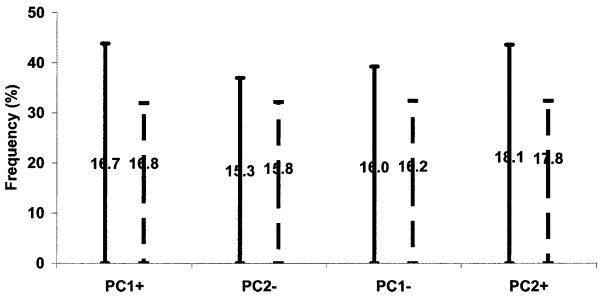

FIG. 13. As in Fig. 7 but for GLA precipitation.

To summarize, it is difficult to make an exact comparison between the GPCP and GLA results since the time resolution and data record are different. Computational limitations forced us to examine only a 10-yr GLA control. Some of the differences can then be attributed to different time resolutions. We did compute the above analysis using GLA precipitation in pentads. Although the main conclusions are still valid, the small sample size of pentads made specific comparisons more difficult. Overall, there is a realistic representation by the GLA model of occurrences of extremes in tropical convective regions associated with the MJO, although further investigation is necessary to determine the reasons for less model variability in the eastern Indian Ocean. There is evidence that interactive coupled SSTs may significantly enhance intraseasonal variability in this region (Waliser et al. 1999b). The higher frequency of extremes in South America during an active MJO than in quiescent cases is also reasonably well represented, although the model has difficulty in simulating the correct timing of the events. Extremes are more frequently observed in South America when the MJO

convection is in the central Pacific, whereas the model suggests more extremes when convection is in the Indian Ocean or Maritime Continent. Finally, the GLA model has a robust signal in the frequency of extremes in the North Pacific and over the western coast of North America, which somewhat agrees with observational studies using station data. This agreement is not seen in the GPCP analysis, probably as a result of the coarse temporal and spatial resolutions in the satellite data.

7. Potential predictability of extreme precipitation

Some previous studies used numerical weather forecast models to determine that the MJO can modulate forecast skill in the extratropics (Lau and Chang 1992; Hendon et al. 2000; Nogués-Paegle et al. 1998; Jones and Schemm 2000; Ferranti et al. 1990). In a recent work, Jones et al. (2004c) used the GLA model and the same predictability experiments described in section 4 to investigate the MJO to influence on extratropical predictability during boreal winter. Mean anomaly correlations (acc) and standardized root-mean-square errors in the midlatitudes of the Northern Hemisphere (20°–60°N) were computed to assess predictability characteristics. The analyses of 500-hPa geopotential height, 200-hPa streamfunction, and 850-hPa zonal wind components systematically showed larger predictability (a gain of about 2–3 days) during periods of active MJOs as opposed to quiescent episodes of the oscillation. The influence of the MJO was further investigated by examining the mean acc between control and perturbation runs in rainfall over domains in the tropical Indian Ocean and western Pacific, western North America, and eastern South America. They found no statistically significant differences in rainfall predictability between active MJO and quiescent periods.

In this section, we examine the role of the MJO in modulating the potential predictability of extreme precipitation. We consider the predictability experiments during high MJO activity (120 events: 4 phases × 15 cases × 2 perturbations) and the frequency of correct forecasts. We define a correct forecast when the model predicted precipitation above the 75th percentile and the precipitation from the control run was indeed above the 75th percentile. For each experiment, we computed the proportion of correct forecasts of extremes from 1 to 14 days lead time: $P1_{k,m} = c/\tau$, where $k = 1, 4$ is an MJO phase, $m = 1, 30$ is the experiment number for the particular MJO phase, c is the number of correct hits, and $\tau = 14$ is the lead time window. The choice of $\tau = 14$ is based on the predictability limit of synoptic variations in the Northern Hemisphere obtained with the GLA model and discussed in Jones et al. (2004c). Similarly, the proportions of correct forecasts for the low intraseasonal activity or null cases (30 events: 15 cases × 2 perturbations) is written as $P2_m = c/\tau$. We represent as

$$\tilde{P}1_k = \sum_{m=1}^{30} P1_{k,m} \quad \text{and} \quad \tilde{P}2 = \sum_{m=1}^{30} P2_m$$

the total sum of proportions of correct forecasts of extremes. As before, we computed the statistic Z_k [(6) and (7)] and performed a one-tailed statistical test where the null hypothesis is $H0$: $\tilde{P}1_k = \tilde{P}2$ and the alternative is H1: $\tilde{P}1_k > \tilde{P}2$.

Figure 14 shows the test statistic Z_k obtained for each MJO phase. Only grid points that exceeded 90% ($Z_k > 1.645$, light shading) and 95% ($Z_k > 1.960$, dark shading) significance levels are displayed. In the Tropics, several areas in Africa, the Indian Ocean, Indonesia, the western Pacific, and South America exhibit statistically significant differences. This indicates higher success in the prediction of extremes during active MJO than in quiescent periods. Apparently, these tropical regions with high predictability of extremes during an active MJO do not seem to follow obvious relationships with the eastward propagation of the oscillation. Additionally, extensive areas in the subtropics and midlatitudes of the North Pacific, western North America, and a large area in the North Atlantic Ocean show large Z_k values, again suggesting the higher predictability of extremes during an active MJO. To gain more understanding of the differences in the proportions of correct forecasts of extremes during active MJOs and quiescent periods, we computed the average $\tilde{P}1_k$ and $\tilde{P}2$ over the grid points that passed the 90% significance test shown in each panel in Fig. 14. As before, the minimum and maximum values were also recorded (Fig. 15). The mean number of correct forecasts of extremes during an active MJO is nearly twice the correct number of extremes during quiescent phases of the oscillation in those locations in which the MJO influence is statistically significant.

8. Summary and conclusions

The Madden–Julian oscillation is the dominant mode of tropical intraseasonal variability and its role in the coupled ocean–atmosphere system has been noted in many previous studies. Indeed, previous work has identified clear signals relating the activity of the MJO to extreme precipitation over specific geographic locations. This paper first developed an observational analysis to obtain a global view of the relation between the slow eastward propagation of the MJO and occurrences of extreme precipitation during boreal winter. This task, which was addressed with GPCP data, was limited to pentad time resolution to ensure global coverage. The results show higher frequency of extremes in the Indian Ocean, Indonesia, and the western Pacific during periods of active MJO than quiescent episodes of the oscillation, which is consistent with anomalies of convective activity associated with the MJO. Moreover, the eastern part of South America exhibits unambiguous and robust signals of increased frequency of extremes during active MJO situations. Other regions with amplified occur-

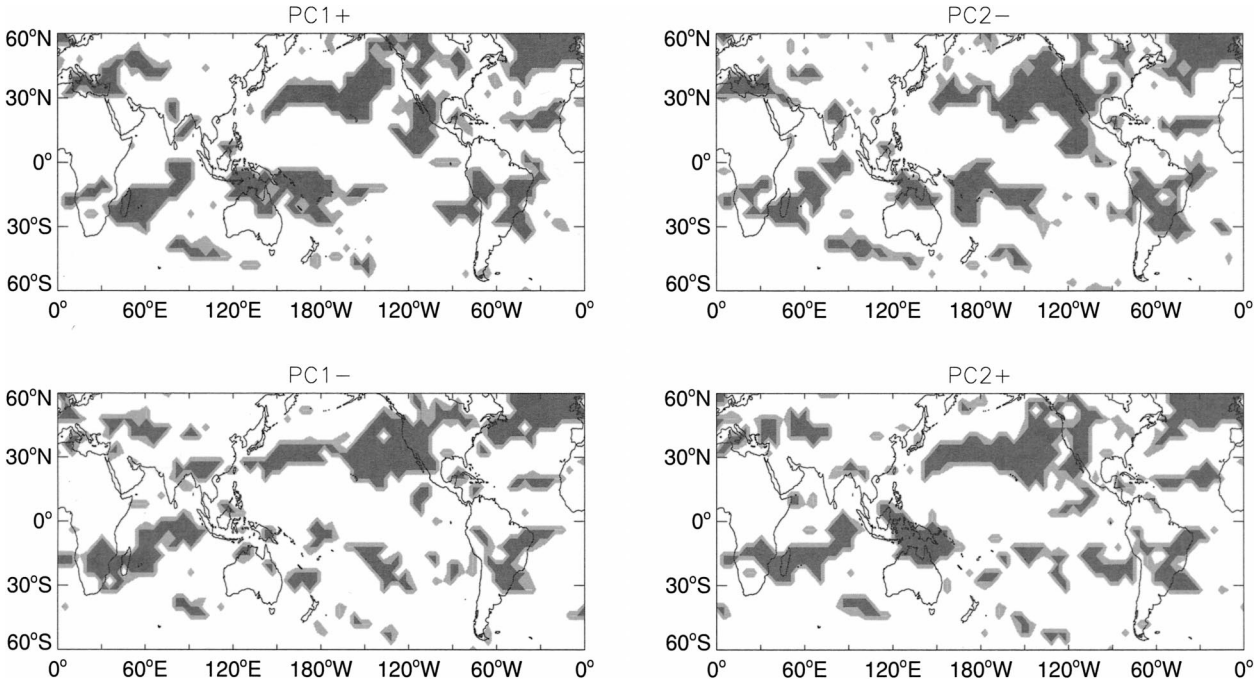

FIG. 14. Test statistic Z_k obtained from predictability experiments. Light (heavy) shading indicates regions statistically significant at the 90% (95%) level where the correct frequency of forecasts of extreme precipitation during active MJOs is higher than in quiescent periods of the oscillation. Only positive Z_k values are shaded (see text for further details).

rence of extremes associated with active MJOs are located over northeast Africa, the Middle East, and eastern China. Although the GPCP data analysis reveals higher frequency of extremes during an active MJO only over some locations off the west coast of North America and parts of southern California, previous studies using surface station data have related the MJO to high frequency of extreme precipitation over western North America. This discrepancy can be partially attributed to the low time and space resolution of the GPCP data, which may be unable to capture the effects of important topographic mesoscale circulations responsible for heavy precipitation in those locations. Nevertheless, the GPCP data analysis indicates that, on a global scale, the number of extreme events during active MJO situations are about 40% higher than in quiescent phases of the oscillation over the locations where the MJO influence is statistically significant.

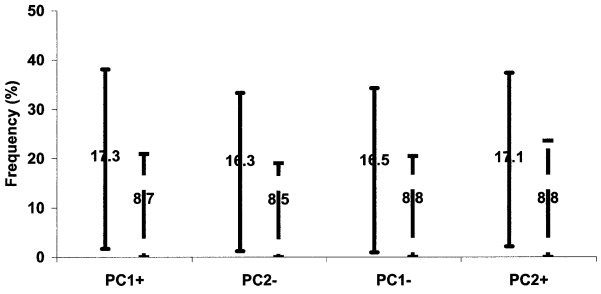

FIG. 15. Mean frequency of correct forecasts. Numbers in the middle of the bars indicate the average $\tilde{P}1_k$ (solid bar) and $\tilde{P}2$ (dashed bar) over the grid points that passed the 90% significance test shown in each panel in Fig. 14. For each phase, the minimum and maximum values are shown as the extremes in the vertical bars.

As a second objective, this paper examined the degree to which the NASA GLA model, which has a relatively reasonable representation of the MJO (e.g., Waliser et al. 2003a,b), realistically simulates the precipitation variability and modulation of the MJO on extreme events. A straight comparison between statistics derived from observed (GPCP) and model (GLA) precipitation is hampered by the different time (and possibly space) resolutions of both datasets. This is an important issue especially when dealing with extreme events. For instance, heavy precipitation in a short period of time (e.g., 1 day) is not necessarily an extreme in 5-day averages. Likewise, steady precipitation during 5 days may not correspond to an extreme when one uses daily resolution. Future improvements in satellite estimates of precipitation (Scofield and Kuligowski 2003) will facilitate the validation of model results. Nevertheless, there is a generally realistic representation by the GLA model of extremes in tropical convective regions associated with the MJO. The higher frequency of extremes in South America during active MJO than in quiescent cases is also reasonably well represented, although the model has difficulty in simulating the timing of the events. The GLA model also shows a strong signal in the frequency of extremes in the North Pacific and

in the western coast of North America, which somewhat agrees with observational studies using station data.

Finally, some previous work has also found that the MJO seems to modulate weather forecast skill in midlatitudes particularly during boreal winter (Lau and Chang 1992; Hendon et al. 2000; Nogués-Paegle et al. 1998; Jones and Schemm 2000; Ferranti et al. 1990). In the third objective of this study, we investigated the relationships between the MJO and the potential predictability of extreme precipitation. The statistical analysis indicates higher success in the prediction of extremes during active MJO than in quiescent situations in several areas in tropical Africa, the Indian Ocean, Indonesia, the western Pacific, and South America. Additionally, extensive areas in the subtropics and midlatitudes of the North Pacific, western North America, and a large area in the North Atlantic Ocean, show increased predictability of extremes during an active MJO. Overall, the predictability experiments indicate the mean number of correct forecasts of extremes during active MJO to be nearly twice the correct number of extremes during quiescent phases of the oscillation in locations where the MJO influence is statistically significant. These results raise encouraging perspectives for further improvements in weather forecasts on subseasonal time scales. Numerical weather prediction models with realistic representation of the MJO as well as empirical forecast models (Waliser et al. 1999a; Lo and Hendon 2000; Mo 2001; Jones et al. 2004b; Wheeler and Weickmann 2001; Wheeler and Hendon 2004) can potentially use the slow eastward propagation of the MJOs to improve the prediction of extreme events at long lead times.

It is also important to recognize a number of caveats associated with the results derived from the numerical model used in this study. First, while the intraseasonal peak of equatorial wavenumber-1, upper-level velocity potential, and zonal wind in the model is quite similar in terms of magnitude and frequency to observations, the model spectra has too much high-frequency (~days) variability for wavenumber 1. Relative to the MJO, this variability would be considered to be unorganized, that is, errant convective activity that may erode the relatively smooth evolution of the MJO. Second, the simulations were carried out with fixed climatological SST values. A previous study with this model showed that coupled SSTs tend to have an enhancing and organizing influence on the MJO, making it stronger and more coherent (Waliser et al. 1999b), which can potentially impact the occurrences of extreme precipitation in the extratropics. The third aspect is the fact that the model contains too little variability over the western Indian Ocean and southern Maritime Continent region. We are currently developing simulations similar to the ones presented here but with coupled SSTs as well as interannual variations.

Acknowledgments. The authors would like to thank Dr. C. Jakob (editor) and the anonymous reviewers for their comments and suggestions to improve the original version of this study. We also acknowledge the support of research grants: C. Jones, National Science Foundation (ATM-0094387) and NOAA Office of Global Programs CLIVAR—Pacific Program (NA16GP1019); and D. E. Waliser, National Science Foundation (ATM-0094416) and NOAA Office of Global Programs CLIVAR (NA16GP2021). The authors would like to thank the Climate Prediction Center (CPC/NCEP/NWS/NOAA) for the GPCP data.

REFERENCES

Arakawa, A., and W. H. Schubert, 1974: Interaction of a cumulus cloud ensemble with the large-scale environment. Part I. *J. Atmos. Sci.,* **31,** 674–701.

Bell, G. D., and M. S. Halpert, 1998: Climate assessment for 1997. *Bull. Amer. Meteor. Soc.,* **79,** 51–550.

Bond, N. A., and G. A. Vecchi, 2003: The Influence of the Madden–Julian oscillation on precipitation in Oregon and Washington. *Wea. Forecasting,* **18,** 600–613.

Carvalho, L. M. V., C. Jones, and B. Liebmann, 2004: The South Atlantic convergence zone: Intensity, form, persistence, and relationships with intraseasonal to interannual activity and extreme rainfall. *J. Climate,* **17,** 88–108.

Cayan, D. R., K. T. Redmond, and L. G. Riddle, 1999: ENSO and hydrologic extremes in the western United States. *J. Climate,* **12,** 2881–2893.

Duchon, C. E., 1979: Lanczos filter in one and two dimensions. *J. Appl. Meteor.,* **18,** 1016–1022.

Ferranti, L., T. N. Palmer, F. Molteni, and K. Klinker, 1990: Tropical–extratropical interaction associated with the 30–60 day oscillation and its impact on medium and extended range prediction. *J. Atmos. Sci.,* **47,** 2177–2199.

Gates, W. L., and A. B. Nelson, 1975: Terrain heights. Part 1. A new (revised) tabulation of the Scripps topography on a one-degree global grid. Tech. Rep. R-1276-1-ARPA, The Rand Corporation, Santa Monica, CA, 132 pp.

Gruber, A., X. Su, M. Kanamitsu, and J. Schemm, 2000: The comparison of two merged rain gauge–satellite precipitation datasets. *Bull. Amer. Meteor. Soc.,* **81,** 2631–2644.

Harshvardhan, R. Davies, D. A. Randall, and T. G. Corsetti, 1987: A fast radiation parameterization for general circulation models. *J. Geophys. Res.,* **92,** 1009–1026.

Hendon, H. H., and M. L. Salby, 1994: The life cycle of the Madden–Julian oscillation. *J. Atmos. Sci.,* **51,** 2225–2237.

——, B. Liebmann, M. Newman, J. D. Glick, and J. Schemm, 2000: Medium-range forecast errors associated with active episodes of the Madden–Julian oscillation. *Mon. Wea. Rev.,* **128,** 69–86.

Higgins, R. W., and W. Shi, 2001: Intercomparison of the principal modes of interannual and intraseasonal variability of the North American monsoon system. *J. Climate,* **14,** 403–417.

——, J.-K. E. Schemm, W. Shi, and A. Leetmaa, 2000: Extreme precipitation events in the western United States related to tropical forcing. *J. Climate,* **13,** 793–820.

Hirose, M., and J. E. Kutzbach, 1969: An alternate method for eigenvector computations. *J. Appl. Meteor.,* **8,** 701.

Houghton, J. T., Y. Ding, D. J. Griggs, M. Nouguer, P. J. van der Linden, X. Dai, K. Maskell, and C. A. Johnson, Eds., 2001: *Climate Change: The Scientific Basis.* Cambridge University Press, 881 pp.

Huffman, G. J., and Coauthors, 1997: The Global Precipitation Project (GPCP) combined precipitation dataset. *Bull. Amer. Meteor. Soc.,* **78,** 5–20.

Jones, C. 2000: Occurrence of extreme precipitation events in Cal-

ifornia and relationships with the Madden–Julian oscillation. *J. Climate,* **13,** 3576–3587.
——, and J.-K. E. Schemm, 2000: The influence of intraseasonal variations on medium-range weather forecasts over South America. *Mon. Wea. Rev.,* **128,** 486–494.
——, and L. M. V. Carvalho, 2002: Active and break phases in the South American monsoon system. *J. Climate,* **15,** 905–914.
——, D. E. Waliser, and C. Gautier, 1998: The influence of the Madden–Julian oscillation on ocean surface heat fluxes and sea surface temperature. *J. Climate,* **11,** 1057–1072.
——, L. M. V. Carvalho, W. Higgins, D. Waliser, and J.-K. Schemm, 2004a: Climatology of tropical intraseasonal convective anomalies: 1979–2002. *J. Climate,* **17,** 523–539.
——, ——, ——, ——, and ——, 2004b: A statistical forecast model of tropical intraseasonal convective anomalies. *J. Climate,* **17,** 2078–2095.
——, D. E. Waliser, K. M. Lau, and W. Stern, 2004c: The Madden–Julian oscillation and its impact on Northern Hemisphere weather predictability. *Mon. Wea. Rev.,* **132,** 1462–1471.
Kalnay, E., R. Balgovind, W. Chao, D. Edelmann, J. Pfaendtner, L. Takacs, and K. Takano, 1983: Documentation of the GLAS fourth-order general circulation model. Vol. 1, NASA Tech. Memo. 86064, NASA Goddard Space Flight Center, Greenbelt, MD, 436 pp.
Lau, K. M., and P. H. Chan, 1986: Aspects of the 40–50 day oscillation during the northern summer as inferred from outgoing longwave radiation. *Mon. Wea. Rev.,* **114,** 1354–1367.
——, and F. C. Chang, 1992: Tropical intraseasonal oscillation and its prediction by the NMC operational model. *J. Climate,* **5,** 1365–1378.
Liebmann, B., C. Jones, and L. M. V. Carvalho, 2001: Interannual variability of extreme precipitation events in the state of São Paulo, Brazil. *J. Climate,* **14,** 208–218.
——, G. N. Kiladis, C. S. Vera, A. C. Saulo, and L. M. V. Carvalho, 2004: Subseasonal variations of rainfall in South America in the vicinity of the low-level jet east of the Andes and comparison to those in the South Atlantic convergence zone. *J. Climate,* **17,** 3829–3842.
Lo, F., and H. H. Hendon, 2000: Empirical prediction of the Madden–Julian oscillation. *Mon. Wea. Rev.,* **128,** 2528–2543.
Lord, S. J., and A. Arakawa, 1980: Interaction of a cumulus cloud ensemble with the large-scale environment. Part II. *J. Atmos. Sci.,* **37,** 2677–2962.
Madden, R. A., and P. R. Julian, 1994: Observations of the 40–50-day tropical oscillation: A review. *Mon. Wea. Rev.,* **122,** 814–837.
Maloney, E. D., and D. L. Hartmann, 1998: Frictional moisture convergence in a composite life cycle of the Madden–Julian oscillation. *J. Climate,* **11,** 2387–2403.
Mo, K. C., 2000: Intraseasonal modulation of summer precipitation over North America. *Mon. Wea. Rev.,* **128,** 1490–1505.
——, 2001: Adaptive filtering and prediction of intraseasonal oscillations. *Mon. Wea. Rev.,* **129,** 802–817.
——, and R. W. Higgins, 1998: Tropical influences on California precipitation. *J. Climate,* **11,** 412–430.
Nogués-Paegle, J., K. Mo, and J. Paegle, 1998: Predictability of the NCEP–NCAR reanalysis model during austral summer. *Mon. Wea. Rev.,* **126,** 3135–3152.
——, L. A. Byerle, and K. Mo, 2000: Intraseasonal modulation of South American summer precipitation. *Mon. Wea. Rev.,* **128,** 837–850.
Phillips, T. J., 1996: Documentation of the AMIP models on the World Wide Web. *Bull. Amer. Meteor. Soc.,* **77,** 1191–1196.
Pielke, R. A., Jr., and M. W. Downton, 2000: Precipitation and damaging floods: Trends in the United States, 1932–97. *J. Climate,* **13,** 3625–3637.
Preisendorfer, R. W., 1988: *Principal Component Analysis in Meteorology and Oceanography.* Developments in Atmospheric Science, Vol. 17, Elsevier, 425 pp.
Scofield, R. A., and R. J. Kuligowski, 2003: Status and outlook of operational satellite precipitation algorithms for extreme-precipitation events. *Wea. Forecasting,* **18,** 1037–1051.
Shapiro, R., 1970: Smoothing, filtering and boundary effects. *Rev. Geophys. Space Phys.,* **8,** 359–387.
Slingo, J. M., and Coauthors, 1996: Intraseasonal oscillations in 15 atmospheric general circulation models: Results from an AMIP diagnostic subproject. *Climate Dyn.,* **12,** 325–357.
Sperber, K. R., J. M. Slingo, P. M. Inness, and K.-M. Lau, 1996: On the maintenance and initiation of the intraseasonal oscillation in the NCEP/NCAR reanalysis and the GLA and UKMO AMIP simulations. *Climate Dyn.,* **13,** 769–795.
Sud, Y. C., and G. K. Walker, 1992: A review of recent research on improvement of physical parameterizations in the GLA GCM. *Physical Processes in Atmospheric Models,* D. R. Sikka and S. S. Singh, Eds., Wiley Eastern, 422–479.
Waliser, D. E., N. E. Graham, and C. Gautier, 1993: Comparison of the highly reflective cloud and outgoing longwave datasets for use in estimating tropical deep convection. *J. Climate,* **6,** 331–353.
——, C. Jones, J. K. Schemm, and N. E. Graham, 1999a: A statistical extended-range tropical forecast model based on the slow evolution of the Madden–Julian oscillation. *J. Climate,* **12,** 1918–1939.
——, K. M. Lau, and J.-H. Kim, 1999b: The influence of coupled sea surface temperatures on the Madden–Julian oscillation: A model perturbation experiment. *J. Atmos. Sci.,* **56,** 333–358.
——, W. Stern, S. Schubert, and K. M. Lau, 2003a: Dynamic predictability of intraseasonal variability associated with the Asian summer monsoon. *Quart. J. Roy. Meteor. Soc.,* **129,** 2897–2925.
——, K. M. Lau, W. Stern, and C. Jones, 2003b: Potential predictability of the Madden–Julian oscillation. *Bull. Amer. Meteor. Soc.,* **84,** 33–50.
Wang, B., and H. Rui, 1990: Synoptic climatology of transient tropical intraseasonal convection anomalies. *Meteor. Atmos. Phys.,* **44,** 43–61.
Weickmann, K. M., G. R. Lussky, and J. E. Kutzbach, 1985: Intraseasonal (30–60 day) fluctuations of outgoing longwave radiation and 250 mb streamfunction during northern winter. *Mon. Wea. Rev.,* **113,** 941–961.
Wheeler, M., and K. Weickmann, 2001: Real-time monitoring and prediction of modes of coherent synoptic to intraseasonal tropical variability. *Mon. Wea. Rev.,* **129,** 2677–2694.
——, and H. H. Hendon, 2004: An all-season real-time multivariate MJO index: Development of an index for monitoring and prediction. *Mon. Wea. Rev.,* **132,** 1917–1932.
Wilks, D. S., 1995: *Statistical Methods in the Atmospheric Sciences.* Academic Press, 464 pp.
Yasunari, T., 1979: Cloudiness fluctuations associated with the Northern Hemisphere monsoon. *J. Meteor. Soc. Japan,* **58,** 225–229.